CVD growth of self-assembled 2D and 1D WS$_2$ nanomaterials for the ultrasensitive detection of NO$_2$

Aanchal Alagh,[+a] Fatima Ezahra Annanouch,[+a] Polona Umek,[b] Carla Bittencourt,[c] Ayrton Sierra-Castillo,[d] Emile Haye,[e] Jean François Colomer[*d] and Eduard Llobet[*a]

[a.] Departament d'Enginyeria Electrònica, Universitat Rovira i Virgili, Països Catalans 26, 43007 Tarragona, Spain.
[b.] Condensed Matter Physics Department, Jožef Stefan Institute, Jamova cesta 39, 1000 Ljubljana, Slovenia.
[c.] Laboratory of Plasma-Surface Interaction Chemistry (PSI Chem), University of Mons, Av. Nicolas Copernic 1, 7000 Mons, Belgium.
[d.] Research Group on Carbon Nanostructures (CARBONNAGe), Namur Institute of Structured Matter (NISM), University of Namur, 61 Rue de Bruxelles, 5000 Namur, Belgium.
[e.] Laboratoire d'Analyse par Réaction Nucléaires (LARN), Namur Institute of Structured Matter (NISM), University of Namur, 61 Rue de Bruxelles, 5000 Namur, Belgium.
+ Authors with equal contributions to this work.

Corresponding Author

*Eduard Llobet, E-mail: eduard.llobet@urv.cat

*Jean-François Colomer: jean-francois.colomer@unamur.be

Abstract:

Herein, we report for the first time on the facile synthesis of 2D layered WS$_2$ nanosheets assembled on 1D WS$_2$ nanostructures by combining the aerosol assisted chemical vapor deposition (AA-CVD) method with H$_2$-free atmospheric pressure CVD, for an ultrasensitive detection of NO$_2$. This synthesis strategy allows us a direct integration of the sensing material onto the sensor transducer with high growth yield and uniform coverage. Two different WS$_2$ morphologies (nanotriangles and nanoflakes) were prepared and investigated. The results show that the assembly of layered WS$_2$ nanosheets on a 3D architecture leads to an improvement in sensing performance by maintaining a high surface area in an accessible porous network. The sensors fabricated show stable, reproducible and remarkable responses towards NO$_2$ at ppb concentration levels. The highest sensitivity was recorded for WS$_2$ NT sensors, with an unprecedented ultra-low detection limit under 5 ppb. Additionally, this material has

demonstrated its ability to detect 800 ppb of NO_2 even when operated at room temperature (25ºC). Regarding humidity cross-sensitivity, our WS_2 sensors remain stable and functional for detecting NO_2 at ppb levels (i.e., a moderate response decrease is observed) when ambient humidity is raised to 50 %. An 8-month long-term stability study has been conducted, which indicates that WS_2-NT sensors show a very stable response to NO_2 over time.

Keywords: gas sensor, AACVD, CVD, WS_2, TMDs.

1. Introduction

Anthropogenic air pollutants are having a negative impact in human health, since these are responsible for about 4.2 million premature deaths yearly, according to the World Health Organization.[1] Premature deaths related to ambient air pollution, occur mainly from heart disease, chronic obstructive pulmonary disease, lung cancer etc. For instance, nitrogen oxides (NO_x) and, particularly, NO_2 are among the five major pollutants that degrade ambient air quality. NO_x are generated from combustion processes, e.g. motor vehicle exhausts. NO_2 has a direct contribution to the formation of ground level ozone in the stratosphere, acid rain and inorganic ambient particulate matter.[2–5] Exposure to NO_2 may cause respiratory irritation, chronic bronchitis, and asthma (53 ppb set as the annual standard by the U.S. Environmental Protection Agency).[6]

The continuous and widespread monitoring of nitrogen dioxide would require using inexpensive sensing technologies. Nowadays, metal oxide chemoresistors or electrochemical cells are commercially available technologies for detecting NO_2.[4,6–9] However, the reliable and selective detection of nitrogen dioxide at ppb levels is still far from what currently marketed inexpensive sensors can offer. Therefore, it is crucially important to develop a new generation of reliable, accurate and cost-effective gas sensors that can detect and monitor in real time low concentrations of NO_2 for air-quality monitoring and human health protection.

Inspired by the intensive research efforts devoted to the application of graphene nanomaterials for gas sensing,[10–13] 2D layered transition metal dichalcogenides (TMDs) materials have been receiving increasing attention and are becoming the target of research in gas sensing.[14–17] 2D TMDs consist of a metal atomic layer sandwiched between two atomic layers of a chalcogen material (e.g. S, Se, Te). TMDs often appear as many 2D layers stacked one above the other by Van der Waals forces of interaction.[14]

Owing to their semiconducting properties, nanoscale thickness and large specific surface area, TMDs hold promise for addressing sensitivity, selectivity, stability and speed (response-recovery time) issues often encountered in gas sensitive materials.[18–20] Indeed, the thinning of the bulk material to a single or few layers leads to a drastic change of its inherent semiconductor properties, primarily due to the confinement of charge carriers in two dimensions (x- and y-directions) due to the low or absence of interactions in the z-direction.[18]

Among the TMDs materials that have demonstrated their usefulness in gas sensing application, WS_2, MoS_2 and SnS_2 are the most studied.[21–25] They have shown promising results towards various gases and vapors of VOCs, at very low operating temperatures. Additionally, TMDs could be used as a scaffold material to which functional groups or complex molecules could be grafted to tune selectivity, employing different approaches such as plasma treatment, low-energy ion implantation/ substitutional doping, covalent or non-covalent functionalization. Such materials can be obtained by means of different routes including chemical or electrochemical Li-interaction and exfoliation,[26–28] a mechanical cleavage method,[24] liquid-phase exfoliation,[29] chemical vapor deposition (CVD),[30] and a wet-chemical method.[31]

Despite the past and current efforts to refine the sensing properties of these new materials and facilitate their integration to obtain functional gas sensor devices, TMDs are still facing

many shortcomings such as low production yield, difficulties for their integration in standard transducing substrates and weak gas response. In fact, the adoption of these novel materials is somewhat limited by the synthesis processes currently employed to grow layered TMDs. As we mentioned above, there are numerous methods available for the synthesis of TMDs, however, they are subject to specific drawbacks. For instance, mechanical exfoliation produces high quality TMDs sheets, but the method cannot be scaled up for mass production, given its extremely low yield. In contrast, if the same sheets are produced via lithium intercalation exfoliation route, yield is substantially increased but with loss of material integrity and alteration of semiconducting properties due to a change in structure caused by lithium ions intercalating in between the exfoliated sheets.[32] Similarly, the production efficiency of TMD nanosheets is high if grown via hydrothermal or solvothermal processes at the cost of losses in crystalline quality. Moreover, most of the growth techniques described above do not allow the direct growth and integration of the desired material onto the sensor transducer, since they are not compatible with a variety of sensor substrates (e.g., ceramics, silicon, silicon MEMS or flexible polymers). Consequently, transfer techniques are needed to remove the material from its growth substrate and to place it onto the application one, which negatively affect fabrication costs as well as the stability of the sensing material (e.g. uncontrolled defects are generated in the transfer process or residues from solvents or polymers remain at the surface after the transfer process is completed). In an attempt to address the issue of poor gas responsiveness, Koo and co-workers reported that gas sensitivity could be ameliorated when the number of the 2D TMDs edges is increased, since higher catalytic activity locates at the edges rather than at the basal plane of the 2D sheets.[15] However, most of the techniques reported lead to the formation of materials with large basal planes and the assembly of 2D TMDs nanosheets into 3D nanostructures remains highly challenging.

Hence, to overcome all the above-mentioned drawbacks, we report for the first time the direct growth on standard ceramic transducers, of a 3D assembly of WS_2 nanosheets on 1D nanostructures, using a two step-CVD (it combines the aerosol-assisted CVD and CVD methods) for developing NO_2 chemoresistive sensors. The nanosheets are grown at atmospheric pressure under argon gas flow without H_2 assistance. This makes the process significantly simple and thermally safe. Two different morphologies were grown in the form of 3D assembly of 2D WS_2 nanoflakes (NFs) and/or nanotriangles (NTs) on WS_2 nanorods and/or nanoneedles respectively. Throughout the paper, these two morphologies are denoted as WS_2 NFs and/or WS_2 NTs respectively. Their phase composition, morphology, microstructure and chemical composition have been characterized. Moreover, the gas-sensing performance of these materials towards NO_2 have been studied under both dry and humid atmospheres. WS_2 NT sensors exhibited very high NO_2 responses with good stability and, an unprecedented low detection limit below 5 ppb at low operating temperature was achieved. Furthermore, the response towards potentially interfering species such as H_2S, H_2 and NH_3 has been studied as well in order to assess NO_2 selectivity. Finally, a discussion on the NO_2 sensing mechanism for the 3D assembly of WS_2 nanosheets is given as well.

2. Experimental Section

2.1. Material synthesis:

First step deposition: either WO_3 nanorods (NRs) or nanoneedles (NNs) were deposited directly on alumina substrates (Pt-interdigitated electrodes with a gap of 300 μm on the front side and Pt- resistive heater meander on the backside, the electrode area was 2.5 mm × 2.5 mm), via AACVD (Fig. 1a) using tungsten hexacarbonyl $W(CO)_6$ (50 mg, purity 97%) dissolved in a mixture of acetone and methanol in a ratio of 3:1. It is worth noting that by changing the nitrogen flow during the AACVD deposition, the obtained morphology can be

varied from NRs to NNs. First, the substrates were cleaned with acetone, ethanol and distilled water, dried with air and then placed inside a CVD hot wall reactor. Next, the precursor along with the organic solvents were mixed in a glass flask, sonicated for 20 minutes and then placed in an ultrasonic bath, to convert the mixture to an aerosol. The deposition temperature was set to 400 °C. Nitrogen gas was used as a carrier gas (0.5 L/min to obtain NRs and 1 L/min to obtain NNs), in order to transport the aerosol to the heated zone inside the reactor. The duration of the complete growth process was kept under 45 minutes. After deposition, the samples were subjected to annealing at 500°C for 3h in dry, zero-grade air at a flow rate of 2 L/min.

Second step deposition: WS_2 was synthesized via the sulfurization of the previously grown WO_3 nanomaterial films using an atmospheric pressure CVD technique, as shown in Fig. 1b. For the two different morphologies of WO_3 nanostructures, the same method of sulfurization was adopted. For sulfurization of WO_3, S powders (99.5%), purchased from Alfa Aesar were used without any further purification. Prior to the sulfurization process, the quartz tube was flushed with 0.725 L/min of argon to remove any oxygen content in the reactor. Two ceramic boats were utilized each one loaded with 0.220 g of sulfur powder. The two boats were placed at different temperature zones of the deposition furnace such that one was positioned at the 40°C temperature zone and the other at 850°C temperature zone (total 0.440 g). WO_3 samples were placed at the 850°C temperature zone in the downstream of the argon flow in the quartz tube reactor. The initial step of sulfurization process goes for a span of 30 minutes wherein the S powder set at the 850°C zone sublimates. The optimized second sulfurization step was performed by inserting the quartz tube in the hot zone of the furnace, such that the S powder which was initially placed at 40°C reaches the 400°C temperature zone. The WO_3 sample remained at 850°C as the quartz reactor was moved over a few centimeters.

2.2. Material characterization techniques

The microstructure of the material was characterized using scanning electron microscopy (SEM-FEI Quanta 600). The chemical analysis has been performed by X-ray photoelectron spectroscopy (XPS), using a K-Alpha Thermo Scientific spectrometer. High-resolution transmission electron microscopy (HRTEM) (Jeol, JEM-2100) was used to analyze crystal structure at the atomic level. XRD measurements were made using a Bruker-AXS D8-Discover diffractometer. Lastly, RAMAN spectroscopy measurements were carried out using Renishaw in Via, laser 514 nm, ion argon-Novatech, 25 mW.

2.3. Gas sensing tests

The gas sensing properties of the different nanomaterials were measured by monitoring the change in electrical resistance of the sensors upon exposure to different target gaseous species (NO_2, NH_3, H_2S, H_2) at different operating temperatures (25°C, 100°C, 150°C). A Teflon test chamber of 35 mL in volume was connected to a fully automated, continuous gas flow measurement set-up able to supply diluted gas mixtures. Sensors were placed inside this test chamber and their electrical resistance was measured using an Agilent-34972A multimeter. To control the operating temperature of a given sensor, its heater was connected to an external power supply (Agilent, model 3492A). The total flow rate was kept constant at a value of 100 mL/min throughout the measurements. Some experiments were conducted under a humid background. Since aging often helps achieving more stable responses, sensors were kept for a week at 150°C under a flow of dry air before their gas sensing properties were investigated.

3. Results and Discussion

3.1. Material synthesis and characterization

Tungsten trioxide NRs and/or NNs were directly deposited on alumina substrate using AACVD method. The as-deposited films were strongly adherent to the substrate, with dark blue

color, which changed to light green after annealing (Fig. S1a). The color of the film was again changed to dark black after undergoing the process of sulfurization (Fig. S1b). The morphology of the synthesized material (WO_3 and WS_2) was examined using a scanning electron microscope. Fig. 2a and b show the SEM imaging results of the as-prepared material before it undergoes the sulfurization process. The results demonstrate that the starting material was composed of either thick nanorods with aggregates of nanoparticles at their tips (Fig. 2a) or thin and elongated nanoneedle structures (Fig. 2b). Besides, it is observed that the grown nanostructures are randomly oriented, tilted and with homogeneous distribution over the substrate.

Also, SEM images revealed that the morphology of WO_3 samples (NRs and NNs) changed due to the sulfurization process. These changes can be observed very well from the obtained images, as shown in Fig. 2c–f. It can be seen that WO_3 nanorods were transformed to a 3D assembly of 2D WS_2 NFs on WS_2 NRs, like flower structures with multilayered sheets as petals. In contrast, the WO_3 nanoneedles, were transformed to a 3D assembly of large WS_2 triangle-shaped crystals (NTs) on WS_2 nanoneedles. Furthermore, a consistent change in color for both deposited films is observed, which clearly indicates the formation of homogeneous and uniform film of WS_2. Thus, the final morphology of the WS_2 materials strongly depends on the morphology of the starting WO_3.

WS_2 samples were investigated by using X-ray powder diffraction (XRD). The XRD diffractograms of a bare Al_2O_3 substrate was compared to those of WO_3 nanorods or WS_2 (coating Al_2O_3 substrates) in view of checking for the presence of tungsten oxide in sulfurized samples. Fig. 3 shows an XRD spectrum for WS_2 NFs. From the spectrum, it is clear that many reflection peaks can be perfectly indexed to the hexagonal P63/*mmc* space group, indicating that the structure of the WS_2 phase is 2H-WS_2 [33]. Besides, we noticed the presence of peaks belonging to alumina substrate.[34] Moreover, XRD did not detect any peaks corresponding to

WO$_3$ impurities. Equivalent results were observed for WS$_2$ NT films (see Fig. S2, Supporting Information).

X-ray spectroscopy (XPS) was used to investigate the chemical states and stoichiometry of WO$_3$ and WS$_2$ films. Fig. 4 depicts an example of the W 4f, S 2p and O 1s core level spectra recorded for the WO$_3$ NNs, WS$_2$ NTs and WS$_2$ NFs. Considering the W 4f spectra of WO$_3$ NNs (Fig. 4a), three components are observed that are associated to the W 4f$_{7/2}$ and W 4f$_{5/2}$ spin orbit doublet, and a low intensity peak originating from the W 5p$_{3/2}$ core level. For the WO$_3$ NNs, the W4f doublet is centered at 35.4 eV and 37.5 eV and the W 5p weak peak around 41 eV. These values are in good agreement with those found in the literature for W^{+6} in WO$_3$ stoichiometric films [35]. The W 4f spectrum can be properly fitted by a doublet, confirming the nature of WO$_3$ material with W only present in the six-valent state. Moreover, one can note the presence of oxygen and the absence of sulfur on this material. Concerning the WS$_2$ NTs and WS$_2$ NFs, the same features that are observed in the WO$_3$ can be observed with a binding energy shift of the different components. Here, the W4f doublet is centered at 32.7 eV and 34.8 eV and the W 5p weak peak around 38.2 eV. The perfect fitting of the spectra for both WS$_2$ NTs and WS$_2$ NFs by a doublet confirms the presence of WS$_2$ with values in good agreement with those found in the literature for W^{+6} in WS$_2$ stoichiometric films [35], without the presence of oxide. This is otherwise correlated with the quasi absence of oxygen and the presence of sulfur. Indeed, in the S 2p spectrum, the known doublet peaks, S 2p$_{1/2}$ and S 2p$_{3/2}$ at 163.4 and 162.2 eV, respectively, with a spin–orbit energy separation of 1.2 eV corresponding to WS$_2$ (S^{2-} oxidation state), can be seen in Fig. 4b. The experimental shape is very well fitted by a doublet demonstrating the presence of the unique phase WS$_2$. Considering the O 1s region (Fig. 4c), the difference between the two materials is well visible, with a lower intensity peak of oxygen in the WS$_2$ material around 533 eV, most likely related to physically adsorbed oxygen molecules. This can be compared to O 1s core level spectrum of WO$_3$ material with a main peak at 530.8

eV related to the WO_3 (O^{2-} oxidation state). Based on the XPS analysis, the complete conversion of WO_3 to WS_2 is demonstrated for both morphologies (at least for the sample depth probed by XPS, which is considered a surface analysis method), since sulfurized materials show the same stoichiometry than that of a WS_2 single crystal.

The purity of the grown films was studied by using Raman spectroscopy, which is a powerful tool to evaluate the crystal quality [36] and to determine whether a TMD material is monolayer or multilayer. Fig. 5a shows an example of WO_3 NRs Raman spectrum. All the peaks (271 cm^{-1}, 327 cm^{-1}, 715 cm^{-1} and 805 cm^{-1}) are indicative of monoclinic tungsten trioxide phase, which is in a good accordance with our previous reported works.[37–39] Fig. 5b and c indicate the Raman spectra collected from WS_2 NTs and NFs films, respectively. Two important Raman peaks characteristic of 2H-WS_2 were observed in both samples: E^1_{2g} at 348.5 and A_{1g} at 414.5 cm^{-1} associated to WS_2 NTs, and E^1_{2g} at 349 and A_{1g} at 416.8 cm^{-1} appertained to WS_2 NFs. The E^1_{2g} mode corresponds to the in-plane vibration of W and S atoms and the A_{1g} mode indicates vibration of sulfides in out of plane direction.[40,41] The ratio of relative peak intensity $I[E^1_{2g}]/I[A_{1g}]$ for both samples turns out to be 0.89, revealing the formation of multilayered WS_2.[42] In contrast, at 700 cm^{-1} and 803 cm^{-1}, two broad peaks were detected with low intensity compared to WO_3 spectrum, indicating the presence of some WO_3 impurities. These results are indicative that Raman is more sensitive than XRD or XPS for detecting traces of tungsten oxide remnants within the WS_2 films. Additionally, it is clear that the morphology did not affect the composition and crystallinity of the WS_2 material.

Fig. 6 shows an example of TEM and HRTEM images obtained from a WS_2 NT sample. TEM analysis revealed that upon sulfurization of WO_3 nanoneedles (i) transformed to WS_2 nanoneedles (Fig. 6) and (ii) that sulfurization triggered the growth of WS_2 triangular nanosheets from side walls and tips of WS_2 nanoneedles (Fig. 6a and Fig. S3a), Supporting Information). Beside nanoneedles also nanotubes with diameters up to 20 nm were observed

(Fig. S3b). The HRTEM image of a triangular WS_2 nanosheet with its corresponding FFT pattern show the hexagonal lattice structure with lattice d-spacing of 0.28 nm corresponding to the 2H-WS_2 (100) planes (PDF pattern 84-1398) (Fig. 6b). HRTEM images of the WS_2 nanoneedles tip and its sidewall (Fig. 6c and d) reveal the (002) crystal plane distances are expanded in comparison to the distance of 0.616 nm in PDF pattern 84-1398. For instance, d-spacings of (002) planes decrease from the outer side toward the inner part of the nanorod (Fig. 6d) from 0.68 to 0.62 nm. The lattice expansion may be connected to crystallographic defects, especially dislocations in the nanoneedles (see red arrows in Fig. 6c and d) [43,44]. TEM analysis did not reveal the presence of WO_3 impurities in the WS_2 materials.

Thus, XRD, XPS, and HRTEM results show good accordance in between them and support the total transformation of WO_3 nanomaterials to WS_2 ones. Moreover, these results were similar for the two morphologies (NFs and NTs) achieved. This apparent discrepancy with Raman results in which the presence of tungsten oxide traces are detected can be explained as follows. XPS is a method that only probes the surface of the sample while XRD and Raman probe the entire sample. Raman is far more sensitive than XRD. All these results taken together are indicative that some tungsten oxide traces remain in the core of the material.

3.2. Gas Sensing Results and Discussion

The gas sensing performances of WS_2 NF or WS_2 NT sensors were examined towards different concentrations of NO_2 and other species such as H_2S, H_2 and NH_3. For all direct-current resistance measurements, the target gas was injected for 10 min into the test chamber where sensors were placed, which was followed by 50 min purging with a dry air flow for sensors to regain their initial baseline resistances. The equation used to calculate sensor response is as follows:

$$R = \frac{(R_{air} - R_{gas})}{R_{air}} * 100$$

Eq.1

To study the effect of the operating temperature on sensor behavior, various NO_2 gas measurements were performed at temperatures ranging from 25 °C to 150 °C. Fig. 7, panels a) and b) depict the intensity of sensor responses as a function of the operating temperature. It is observed that sensor response for both morphologies, WS_2 NFs as well as WS_2 NTs increased almost linearly with the increase in operating temperature. This can be explained well by enhanced adsorption of gas molecules at higher temperatures. Indeed, as the temperature is increased the activation barrier is lowered which enhances the rate of gas adsorption on the surface, leading to a much higher response at an elevated temperature. However, measurements beyond 150°C were not performed, since the evaporation of sulfur would start and the formation process of WO_3 will initiate leading to a formation of a WO_3/WS_2 composite. Thus, for subsequent studies, 150°C was considered as the optimal working temperature for both types of sensors. This operating temperature is quite low in comparison to the standard operating temperatures for most metal oxide gas sensors. Fig.7, panels b) an c) show the evolution of the electrical resistance of the sensors operated at 150 °C under repeated exposure and recovery cycles of NO_2. As we can see WS_2 NT films are more resistive than WS_2 NF films, since the baseline resistance of WS_2 NTs is significantly higher than that of WS_2 NFs.

Fig. 8 shows typical repeated response and recovery cycles for WS_2 NF and WS_2 NT sensors towards 800 ppb of NO_2. As it is clear from the figure, sensors show a decrease in their electrical resistance when exposed to NO_2 (i.e., an oxidizing gas), indicating a p-type semiconducting behavior. This can be explained by the spontaneous adsorption of NO_2 gas molecules on the WS_2 surface, thereby withdrawing electrons via the valence band causing an increase in hole

concentration and resulting in an overall decrease in the electrical resistance of the film.[45] Moreover, both sensors show stable, reproducible and remarkable responses towards 800 ppb of NO_2 gas. While the WS_2 NF sensor response is 26.6%, the response of the WS_2 NT sensor is significantly higher and reaches 56%.

Also, the sensors were exposed to consecutive concentration pulses of NO_2 that ranged from 50 to 300 ppb, as depicted in Fig. 9. During these measurements, the two sensor types were tested at five different concentrations of NO_2 at a constant operating temperature of 150°C. A diluted mixture of NO_2 in dry air was injected for 10 minutes in steps of increasing concentrations of 50, 80, 100, 200 and 300 ppb. It is evident from the results obtained that there is an increase in response with each increment in analyte concentration. The WS_2 NF sensor response was calculated to be 0.16%, 0.96%, 2.28%, 3.41%, and 6.69% for 50, 80, 100, 200 and 300 ppb of nitrogen dioxide, respectively. In contrast, the response increased to higher values (19.6%, 38.04%, 39.3%, 40.265, 41.75%) for the WS_2 NTs sensor. Hence, WS_2 NTs are significantly more sensitive to NO_2 than WS_2 NFs. These results encouraged us to investigate the responses of WS_2 NTs towards NO_2 at concentrations lower than 50 ppb.

Fig. 10a and b present the responses of WS_2 NTs towards very low concentrations of NO_2 (5 ppb and 10 ppb) at 150˚C. It is clearly observed that the nanomaterial was able to detect such small concentrations with good responses and enough signal to noise ratio. For 5 ppb and 10 ppb of NO_2 the responses recorded were 3.20% and 7.23% respectively. It is worth noting that no responses above the noise level were obtained from WS_2 NFs at such low concentrations of NO_2. Hence, the detection limit is roughly 50 ppb of NO_2 for WS_2 NFs, while this detection limit is clearly below 5 ppb of NO_2 for WS_2 NTs. Indeed, considering the low noise levels observed in Fig. 10 a, the limit of detection for NO_2 lies in the ppt concentration levels. To the best of our knowledge, none of the reported works in the literature have achieved such a small detection limit of NO_2 gas (below 5 ppb) using a WS_2 nanomaterial. Fig. 10c depicts the

response of WS_2 NTs to pulses of 10 and 20 ppb of nitrogen dioxide. Five consecutive replicate measurement sequences were performed to study repeatability. Similarly, Fig. 10d shows four replicate measurement sequences for concentration pulses ranging from 50 to 800 ppb of NO_2. From these results, it is clear that WS_2 NTs were able to discern between all the concentrations tested. Additionally, sensor responses were remarkably stable and reproducible, which can be attributed to the direct growth of the nanomaterial on the sensor transducer. While all the above-discussed measurements were performed at the operating temperature of 150ºC, Fig. 10e shows the responses towards 800 ppb of NO_2 of WS_2 NTs operated at room temperature. Despite the higher drift experienced in the baseline resistance, surely due to the difficulty of desorbing NO_2 molecules from the surface during the cleaning cycles at room temperature, the nanomaterial was able to detect NO_2 at room temperature with an acceptable and reproducible response of 10.6%. To further study the sensing performance of WS_2 NTs, its behavior in a humid environment was considered as well. The effect of ambient moisture was studied as it is well known that water vapor can affect sensor response by affecting its electrical resistance in a similar way to that of a reducing gas, resulting in an interfering effect for gas detection. Fig. 10f shows three replicate sensor response and recovery cycles towards 800 ppb of NO_2 for a WS_2 NT sensor operated at 150ºC in dry (~3% RH @ 25ºC) and humid (50 % RH @ 25ºC) backgrounds. One can observe that under humid conditions, sensor remains fully functional with good and reproducible response. However, there is a tolerable decrease in response intensity, since response decreased from 56 % to 30 %. It is worth noting that most of the reported studies on layered TMD gas sensors have not studied the effect of ambient humidity on sensing performance, an essential aspect for the real application of gas sensors.

The response towards NH_3, H_2S, H_2 was studied as a way to assess the potential selectivity of the nanomaterials studied in the detection of NO_2. Typical sensor response and recovery signals for these reducing species can be found in Fig. S4. The concentrations tested for these

interfering species were chosen to be much higher than that of the target gas. Fig. 11 summarizes the obtained results. The responses towards these species are negative, because sensor resistance increases in the presence of these electron donor species, which further confirms the p-type behavior of our WS_2 nanomaterials. It is evident from the bar graph that both WS_2 NF and WS_2 NT sensors were highly sensitive and NO_2. NO_2 response is significantly higher than the one recorded for any of the other species tested. Besides, it is noticeable that WS_2 NTs sensor showed high responses to H_2S, however it must be stressed that the concentration tested for hydrogen sulfide was fifty times higher than the one for NO_2. These results are in line with previously reported theoretical studies indicating that the interaction of the NO_2 molecule with the surface of 2D TMDs is characterized by higher adsorption energy and charge transfer than for other molecules such as NH_3 or H_2S [21]. These results indicate that WS_2 sensors show potential for the selective detection of NO_2 traces, provided some surface functionalization is conducted to decrease the current cross-sensitivity experienced.

Based on the obtained results, sensor with large nanotriangular sheets assembled on 1D nanoneedles (WS_2 NTs) displayed the best NO_2 gas sensing performances. This can be attributed to the difference in the morphology, since it can have a huge impact on how gas molecules interact with and get adsorbed on the sensing surface. Further, the material characterization results showed that both nanomaterials are identical in terms of chemical composition and crystallographic phase, whereas the only difference was in their morphologies.

Table 1 summarizes the main results achieved and puts them in context with the state of the art. In this table, the performance in the detection of NO_2 reported here are compared against those in the literature NO_2 gas detection. From these results it is clear that sensors based on WS_2 NTs show very remarkable gas responses with high sensitivity an unprecedented detection limit below 5 ppb for NO_2 gas at 150°C. The long-term stability of the NO_2 sensing properties

for WS$_2$ materials was studied (see the Supporting Information, Fig. S5). It was found that WS$_2$-NTs show a very stable response to NO$_2$ over 8 months of tests.

3.3. NO$_2$ gas sensing mechanism

NO$_2$ molecules behave as electron acceptors and H$_2$S, H$_2$ or NH$_3$ behave as electron donors. The resistance of the WS$_2$ devices decreases in the presence of NO$_2$ and increases in the presence of the above mentioned electron donor species, which is indicative that our multilayer tungsten disulfide behaves as a p-type semiconducting material. While single layer WS$_2$ behaves usually as an n-type semiconductor,[46] the n-type or p-type nature of WS$_2$ depends on its morphology, nanostructure alignment on the substrate or even on the presence of few carbon atoms substituting sulfur atoms.[47] The p-type behavior of WS$_2$ achieved via the sulfurization of WO$_3$ has been reported previously.[48] The nitrogen dioxide sensing mechanism in WS$_2$ NFs or NTs (Fig. 12) involves the adsorption of NO$_2$ molecules both on the edges of flakes or triangles and on their surface (or basal plane). Upon adsorption, electronic charge is injected from WS$_2$ towards the gas molecule, which generates a hole accumulation zone that results in a decrease in the resistance of the film. According to previously reported computational chemistry studies in MoS$_2$, the edges are far more important than the basal plane for the adsorption of NO$_2$, because the adsorption energy of nitrogen dioxide at S edges is higher (~ -0.4 eV) than at the basal plane (~ -0.13 eV) and the associated electronic charge transfer is ~ 0.5 e and 0.1 e, respectively.[49] These adsorption energies suggest that the interaction between WS$_2$ and NO$_2$ would involve the physisorption of nitrogen dioxide. This is supported by the experimental results showing that sensor baseline resistance can be regained when flowing the sensor surface with clean air, even when sensors are operated at room temperature (i.e. 25ºC). It is worth noting that the assembly of WS$_2$ nanotriangles on 1D nanoneedles or nanorods shows a highly increased porosity and increased number of edges for gas interaction

in comparison to the more closely packed nanoflake assembly. This explains the superior gas sensing properties recorded for WS_2 with nanotriangle morphology.

4. Conclusions

We have demonstrated an efficient route to synthesize high quality, multi-layered WS_2 nanosheets homogeneously assembled in 1D nanoneedles or nanorods. The nanomaterials are directly grown onto standard ceramic application transducers for developing chemoresistive gas sensors, using a double step CVD technique. It can be concluded that the final morphology of WS_2 films heavily depends on that of pre-deposited WO_3 layers, which is easily scalable and controllable, making it possible to meet the demands for different applications. Gas sensing results showed that WS_2 NTs exhibited excellent NO_2 gas sensing characteristics at low operating temperature, even at room temperature. The high sensitivity observed and the unprecedentedly low limit of detection achieved (in the ppt range), were attributed to the porous surface and the increased number of sulfur edges in WS_2 NTs, which were created by the random 3D assembly of WS_2 nanosheets on WS_2 nanoneedles. Furthermore, WS_2 NTs have shown an excellent response stability during long-term stability tests conducted over an 8-month period. Hence, these results shed light on the important role played by the morphology in enhancing sensor performance. Furthermore, good stability and reproducibility of the responses were observed as well and these were related to the direct growth of the material on the sensor transducer. Henceforth this study paves a way to develop WS_2 gas sensors with improved quality for NO_2 detection.

Appendix A. Supplementary data

Supplementary material related to this article can be found, in the online version.

Referernces

[1] WHO, Ambient air pollution: Health impacts.

[2] D. Zhang, Z. Liu, C. Li, T. Tang, X. Liu, S. Han, B. Lei, C. Zhou, Detection of NO_2 down to ppb levels using individual and multiple In_2O_3 nanowire devices, Nano Lett. 4 (2004) 1919–1924.

[3] M.E. Munawer, Human health and environmental impacts of coal combustion and post-combustion wastes, J. Sustain. Min. 17 (2018) 87–96.

[4] S.S. Shendage, V.L. Patil, S.A. Vanalakar, S.P. Patil, N.S. Harale, J.L. Bhosale, J.H. Kim, P.S. Patil, Sensitive and selective NO_2 gas sensor based on WO_3 nanoplates, Sens. Actuators, B-chem. 240 (2017) 426–433

[5] W. Zheng, Y. Xu, L. Zheng, C. Yang, N. Pinna, X. Liu, J. Zhang, MoS_2 Van der Waals p–n Junctions Enabling Highly Selective Room-Temperature NO_2 Sensor, Adv. Funct. Mater. n/a (2020) 2000435.

[6] Environmental Protection Agency, Primary National Ambient Air Quality Standards (NAAQS) for Nitrogen Dioxide.

[7] S. Zampolli, I. Elmi, F. Mancarella, P. Betti, E. Dalcanale, G.C. Cardinali, M. Severi, Real-time monitoring of sub-ppb concentrations of aromatic volatiles with a MEMS-enabled miniaturized gas-chromatograph, Sens. Actuators, B-chem. 141 (2009) 322–328.

[8] N. G. Cho, D. J. Yang, M-J. Jin, H-G. Kim, H. L. Tuller, I-D. Kim, Highly sensitive SnO_2 hollow nanofiber-based NO_2 gas sensors, Sens. Actuators, B-chem. 160 (2011) 1468–1472.

[9] A. Falak, Y. Tian, L. Yan, M. Zhao, X. Zhang, F. Dong, P. Chen, H. Wang, W. Chu, Room Temperature Detection of NO_2 at ppb Level and Full Recovery by Effective Modulation of the Barrier Height for Titanium Oxide/Graphene Schottky Heterojunctions, Adv. Funct. Mater. 6 (2019) 1900992.

[10] Z. Song, Z. Wei, B. Wang, Z. Luo, S. Xu, W. Zhang, H. Yu, M. Li, Z. Huang, J. Zang, Sensitive room-temperature H_2S gas sensors employing SnO_2 quantum wire/reduced graphene oxide nanocomposites, Chem. Mater. 28 (2016) 1205–1212.

[11] W. Hyung Cheong, J. Hyeb Song, J. Joon Kim, Wearable, wireless gas sensors using highly stretchable and transparent structures of nanowires and graphene, Nanoscale. 8 (2016) 10591–10597.

[12] S.M. Mortazavi Zanjani, M.M. Sadeghi, M. Holt, S.F. Chowdhury, L. Tao, D. Akinwande, Enhanced sensitivity of graphene ammonia gas sensors using molecular doping, Appl. Phys. Lett. 108 (2016) 033106.

[13] R. Pearce, T. Iakimov, M. Andersson, L. Hultman, A. Lloyd Spetz, R. Yakimova, Epitaxially grown graphene based gas sensors for ultra sensitive NO_2 detection, Sens. Actuators, B-chem. 155 (2011) 451–455.

[14] J. Ping, Z. Fan, M. Sindoro, Y. Ying, H. Zhang, Recent advances in sensing applications of two☐dimensional transition metal dichalcogenide nanosheets and their composites, Adv. Funct. Mater. 27 (2017) 1605817.

[15] W.-T. Koo, J.-H. Cha, J.-W. Jung, S.-J. Choi, J.-S. Jang, D.-H. Kim, I.-D. Kim, Few-Layered WS_2 Nanoplates Confined in Co, N-Doped Hollow Carbon Nanocages: Abundant WS_2 Edges for Highly Sensitive Gas Sensors, Adv. Funct. Mater. 28 (2018) 1802575.

[16] Z. Qin, K. Xu, H. Yue, H. Wang, J. Zhang, C. Ouyang, C. Xie, D. Zeng, Enhanced room-temperature NH3 gas sensing by 2D SnS2 with sulphur vacancies synthesized by chemical exfoliation, Sens. Actuators, B-chem. 262 (2018) 771–779.

[17] Q. He, Z. Zeng, Z. Yin, H. Li, S. Wu, X. Huang, H. Zhang, Fabrication of flexible MoS2 thin film transistor arrays for practical gas sensing applications, Small. 8 (2012) 2994–2999.

[18] X. Li, X. Li, Z. Li, J. Wang, J. Zhang, WS2 nanoflakes based selective ammonia sensors at room temperature, Sens. Actuators, B-chem. 240 (2017) 273–277.

[19] D.J. Late, R.V. Kanawade, P.K. Kannan, C.S. Rout, Atomically thin WS_2 nanosheets based gas sensor, Sens. Lett. 14 (2016) 1249–1254.

[20] C.C. Mayorga-Martinez, A. Ambrosi, A.Y.S. Eng, Z. Sofer, M. Pumera, Metallic 1T-WS2 for Selective Impedimetric Vapor Sensing, Adv. Funct. Mater. 25 (2015) 5611–5616.

[21] J.Z. Ou, W. Ge, B. Carey, T. Daeneke, A. Rotbart, W. Shan, Y. Wang, Z. Fu, A.F. Chrimes, W. Wlodarski, Physisorption-based charge transfer in two-dimensional SnS2 for selective and reversible NO_2 gas sensing, ACS Nano. 9 (2015) 10313–10323.

[22] Y.-H. Kim, D.-T. Phan, S. Ahn, K.-H. Nam, C.-M. Park, K.-J. Jeon, Two-dimensional SnS2 materials as high-performance NO_2 sensors with fast response and high sensitivity, Sens. Actuators, B-chem. 255 (2018) 616–621.

[23] D.J. Late, Y.-K. Huang, B. Liu, J. Acharya, S.N. Shirodkar, J. Luo, A. Yan, D. Charles, U.V. Waghmare, V.P. Dravid, Sensing behavior of atomically thin-layered MoS2 transistors, ACS Nano. 7 (2013) 4879–4891.

[24] M. O'Brien, K. Lee, R. Morrish, N.C. Berner, N. McEvoy, C.A. Wolden, G.S. Duesberg, Plasma assisted synthesis of WS_2 for gas sensing applications, Chem. Phys. Lett. 615 (2014) 6–10.

[25] D. Gu, X. Li, H. Wang, M. Li, Y. Xi, Y. Chen, J. Wang, M.N. Rumyntseva, A.M. Gaskov, Light enhanced VOCs sensing of WS2 microflakes based chemiresistive sensors powered by triboelectronic nangenerators, Sens. Actuators, B-chem. 256 (2018) 992–1000.

[26] K.Y. Ko, J.G. Song, Y. Kim, T. Choi, S. Shin, C.W. Lee, K. Lee, J. Koo, H. Lee, J. Kim, T. Lee, J. Park, H. Kim, Improvement of Gas-Sensing Performance of Large-Area Tungsten Disulfide Nanosheets by Surface Functionalization, ACS Nano. 10 (2016) 9287–9296.

[27] T. Xu, Y. Liu, Y. Pei, Y. Chen, Z. Jiang, Z. Shi, J. Xu, D. Wu, Y. Tian, X. Li, The ultra-high NO_2 response of ultra-thin WS_2 nanosheets synthesized by hydrothermal and calcination processes, Sens. Actuators, B-chem. 259 (2018) 789–796.

[28] W. Yan, M.A. Worsley, T. Pham, A. Zettl, C. Carraro, R. Maboudian, Effects of ambient humidity and temperature on the NO_2 sensing characteristics of WS_2/graphene aerogel, Appl. Surf. Sci. 450 (2018) 372–379.

[29] K.M. McCreary, A.T. Hanbicki, G.G. Jernigan, J.C. Culbertson, B.T. Jonker, Synthesis of large-area WS2 monolayers with exceptional photoluminescence, Sci. Rep. 6 (2016) 19159.

[30] C. Lan, C. Li, Y. Yin, Y. Liu, Large-area synthesis of monolayer WS2 and its ambient-sensitive photo-detecting performance, Nanoscale. 7 (2015) 5974–5980.

[31] S.P. Vattikuti, C. Byon, C.V. Reddy, Synthesis of MoS2 multi-wall nanotubes using wet chemical method with H_2O_2 as growth promoter, Superlattices Microstruct. 85 (2015) 124–132.

[32] J. Sun, X. Li, W. Guo, M. Zhao, X. Fan, Y. Dong, C. Xu, J. Deng, Y. Fu, Synthesis methods of two-dimensional MoS_2: A brief review, Crystals. 7 (2017) 198.

[33] T.A.J. Loh, D.H.C. Chua, A.T.S. Wee, One-step Synthesis of Few-layer WS2 by Pulsed Laser Deposition, Sci. Rep. 5 (2015) 1–9.

[34] P. Arod, S. Shivashankar, Single-step synthesis of carbon nanotubes/iron/iron oxide composite films through inert-ambient CVD using ferric acetylacetonate as a precursor, RSC Adv. 5 (2015) 59463–59471.

[35] K.M. McCreary, A.T. Hanbicki, G.G. Jernigan, J.C. Culbertson, B.T. Jonker, Synthesis of Large-Area WS_2 monolayers with Exceptional Photoluminescence, Sci. Rep. 6 (2016) 1–7.

[36] N.R. Pradhan, D. Rhodes, S. Feng, X. Yan, S. Memaran, M. B.H., H. Terrones, M. Terrones, L. Balicas, Controlled synthesis and transfer of large-area WS_2 sheets: From single layer to few layers, ACS Nano. 7 (2013) 5235–5242.

[37] F.E. Annanouch, Z. Haddi, S. Vallejos, P. Umek, P. Guttmann, C. Bittencourt, E. Llobet, Aerosol-assisted CVD-grown WO_3 nanoneedles decorated with copper oxide nanoparticles for the selective and humidity-resilient detection of H_2S, ACS Appl. Mater. Interfaces 7 (2015) 6842–6851.

[38] F.E. Annanouch, Z. Haddi, M. Ling, F. Di Maggio, S. Vallejos, T. Vilic, Y. Zhu, T. Shujah, P. Umek, C. Bittencourt, Aerosol-assisted CVD-grown PdO nanoparticle-decorated tungsten oxide nanoneedles extremely sensitive and selective to hydrogen, ACS Appl. Mater. Interfaces 8 (2016) 10413–10421.

[39] S. Vallejos, P. Umek, T. Stoycheva, F. Annanouch, E. Llobet, X. Correig, P. De Marco, C. Bittencourt, C. Blackman, Single-Step Deposition of Au- and Pt-Nanoparticle-Functionalized Tungsten Oxide Nanoneedles Synthesized Via Aerosol-Assisted CVD, and Used for Fabrication of Selective Gas Microsensor Arrays, Adv. Funct. Mater. 23 (2013) 1313–1322.

[40] Q. Fu, W. Wang, L. Yang, J. Huang, J. Zhang, B. Xiang, Controllable synthesis of high quality monolayer WS 2 on a SiO_2/Si substrate by chemical vapor deposition, RSC Adv. 5 (2015) 15795–15799.

[41] Y. Rong, Y. Fan, A.L. Koh, A.W. Robertson, K. He, S. Wang, H. Tan, R. Sinclair, J.H. Warner, Controlling sulphur precursor addition for large single crystal domains of WS_2, Nanoscale. 6 (2014) 12096–12103.

[42] J. Park, W. Lee, T. Choi, S.-H. Hwang, J.M. Myoung, J.-H. Jung, S.-H. Kim, H. Kim, Layer-modulated synthesis of uniform tungsten disulfide nanosheet using gas-phase precursors, Nanoscale. 7 (2015) 1308–1313.

[43] M. Krause, A. Mücklich, A. Zak, G. Seifert, S. Gemming, High resolution TEM study of WS2 nanotubes, Phys. Status Solidi (b). 248 (2011) 2716–2719.

[44] V. Weiß, S. Seeger, K. Ellmer, R. Mientus, Reactive magnetron sputtering of tungsten disulfide (WS 2− x) films: Influence of deposition parameters on texture, microstructure, and stoichiometry, J. Appl. Phys. 101 (2007) 103502.

[45] G. Jimenez-Cadena, J. Riu, F.X. Rius, Gas sensors based on nanostructured materials, Analyst. 132 (2007) 1083–1099.

[46] D. Ovchinnikov, A. Allain, Y.-S. Huang, D. Dumcenco, A. Kis, Electrical transport properties of single-layer WS_2, ACS Nano. 8 (2014) 8174–8181.

[47] F. Zhang, Y. Lu, D.S. Schulman, T. Zhang, K. Fujisawa, Z. Lin, Y. Lei, A.L. Elias, S. Das, S.B. Sinnott, Carbon doping of WS_2 monolayers: Bandgap reduction and p-type doping transport, Sci. Adv. 5 (2019) eaav5003.

[48] G.A. Asres, J.J. Baldoví, A. Dombovari, T. Järvinen, G.S. Lorite, M. Mohl, A. Shchukarev, A.P. Paz, L. Xian, J.-P. Mikkola, Ultrasensitive H_2S gas sensors based on p-type WS_2 hybrid materials, Nano Res. 11 (2018) 4215–4224.

[49] G. Deokar, P. Vancsó, R. Arenal, F. Ravaux, J. Casanova☐Cháfer, E. Llobet, A. Makarova, D. Vyalikh, C. Struzzi, P. Lambin, MoS₂–Carbon nanotube hybrid material growth and gas sensing, Adv. Mater Interfaces. 4 (2017) 1700801.

[50] W. Yan, A. Harley-Trochimczyk, H. Long, L. Chan, T. Pham, M. Hu, Y. Qin, A. Zettl, C. Carraro, M.A. Worsley, Conductometric gas sensing behavior of WS₂ aerogel, FlatChem. 5 (2017) 1–8.

[51] D. Liu, Z. Tang, Z. Zhang, Comparative study on NO₂ and H₂S sensing mechanisms of gas sensors based on WS2 nanosheets, Sens. Actuators, B-chem.303 (2020) 127114.
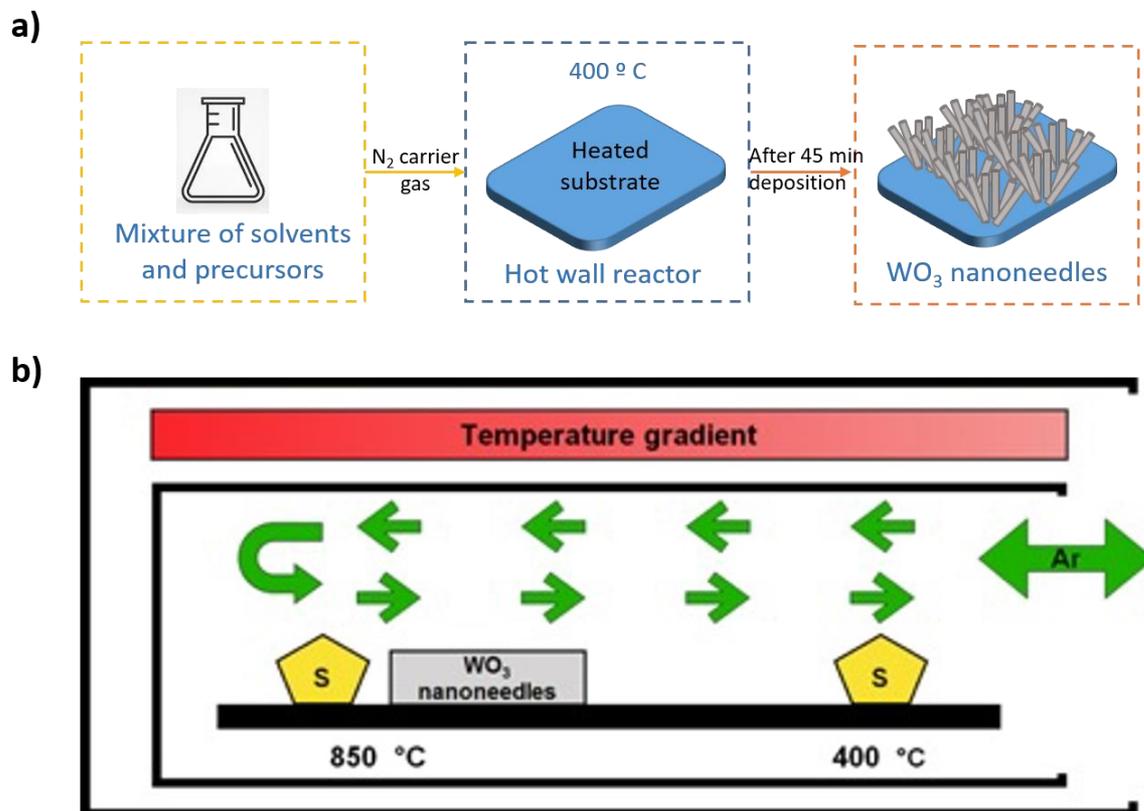
Fig. 1. (a) AACVD synthesis of WO₃ nanomaterials, (b) CVD synthesis of WS₂ nanomaterials.
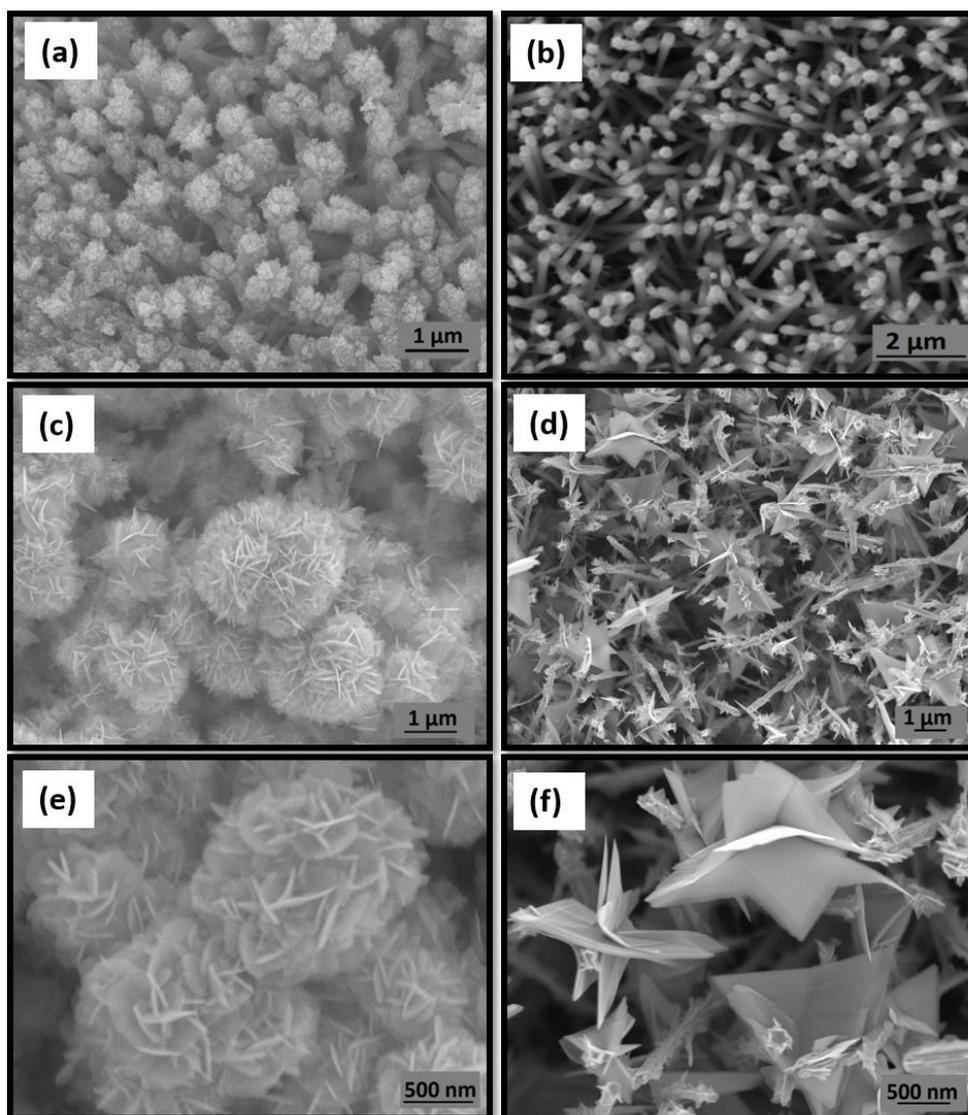
Fig. 2. SEM images of (a) WO_3 nanorods, (b) WO_3 nanoneedles, (c and e) WS_2 nanoflakes and (d and f) WS_2 nanotriangles
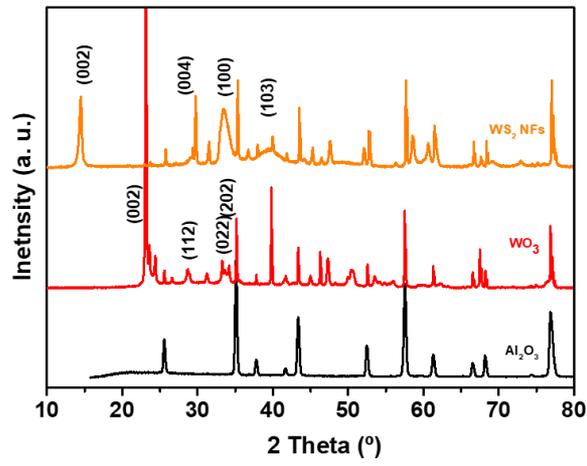
Fig. 3. XRD diffractograms for a bare Al_2O_3 substrate (lower patter), WO_3 NRs (middle pattern and WS_2 NFs (upper pattern).
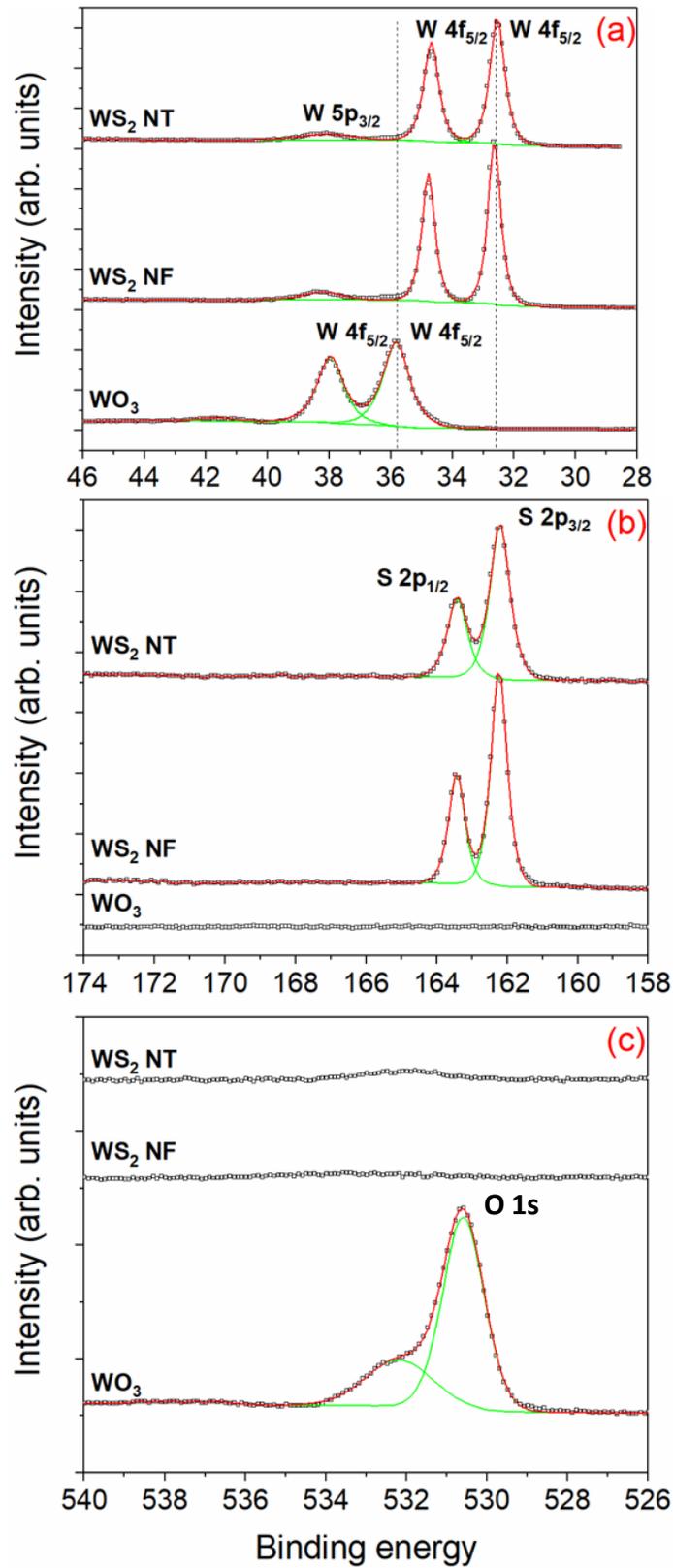
Fig. 4. XPS spectra of the W 4f (a), S 2p (b) and O 1s (c) core levels for WO_3 NNs (before the sulfurization reaction), WS_2 NFs and WS_2 NTs (i.e., after the sulfurization reaction).
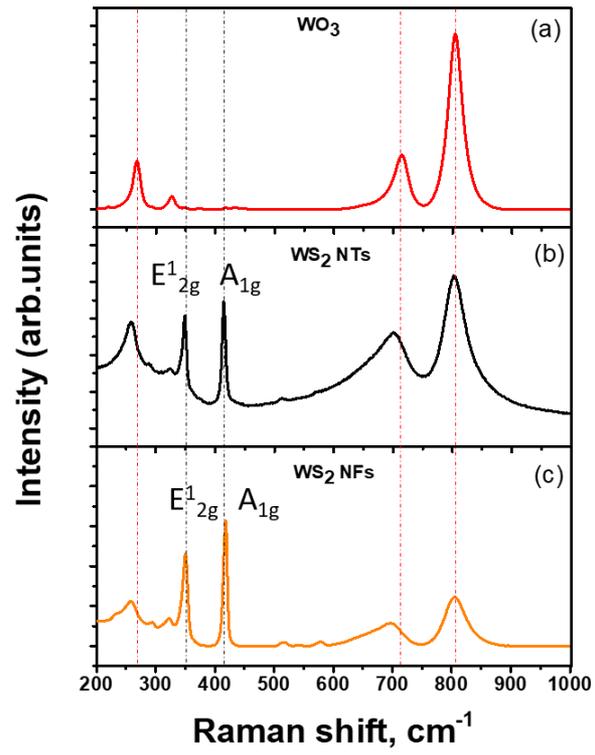
Fig. 5. Raman spectra of (a) WO_3 NRs, (b) WS_2 NTs and (c) WS_2 NFs.
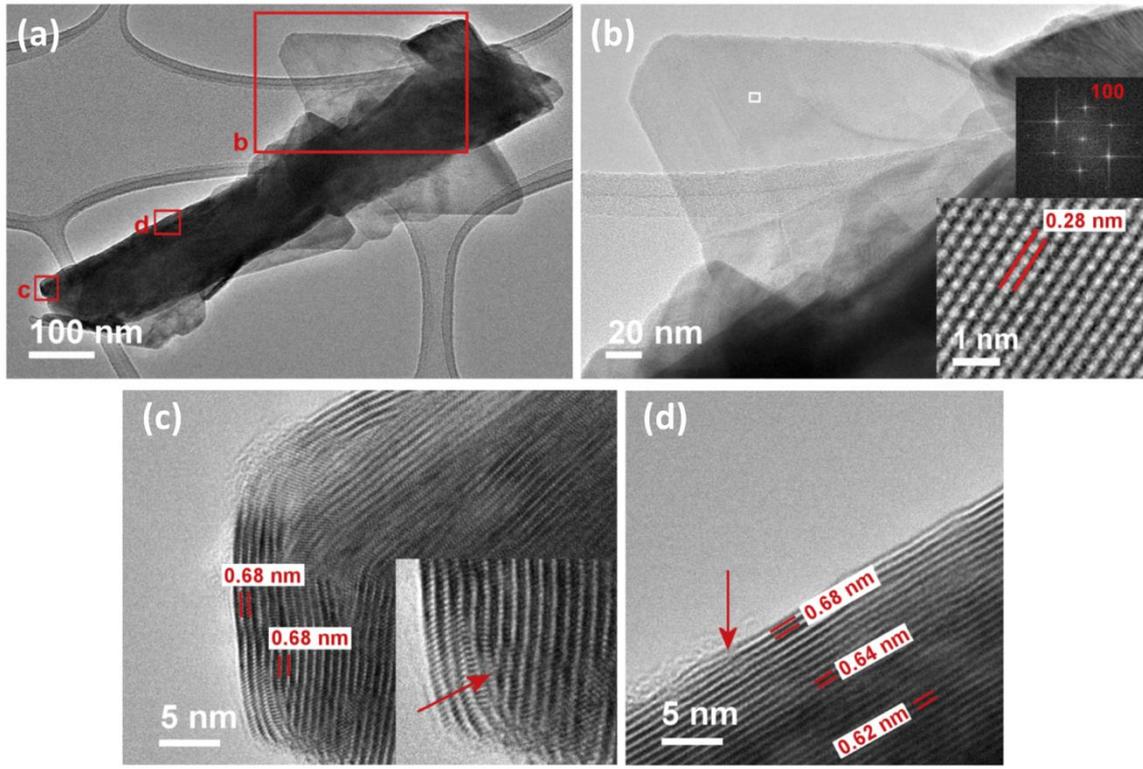
Fig. 6. TEM image of a WS$_2$ nanoneedles (a). Triangular WS$_2$ nanosheet growing from a nanoneedles longest side. The white frame in the image indicates the area where HRTEM image was taken (bottom inset); the upper inset is the corresponding FFT pattern (b). HRTEM images of the WS$_2$ nanoneedle end (c), and sidewall of the WS$_2$ nanoneedle (d). Arrows in panels (c) and (d) are pointing to dislocations. Red frames in panel (a) indicate the areas shown in HRTEM images (b), (c) and (d).
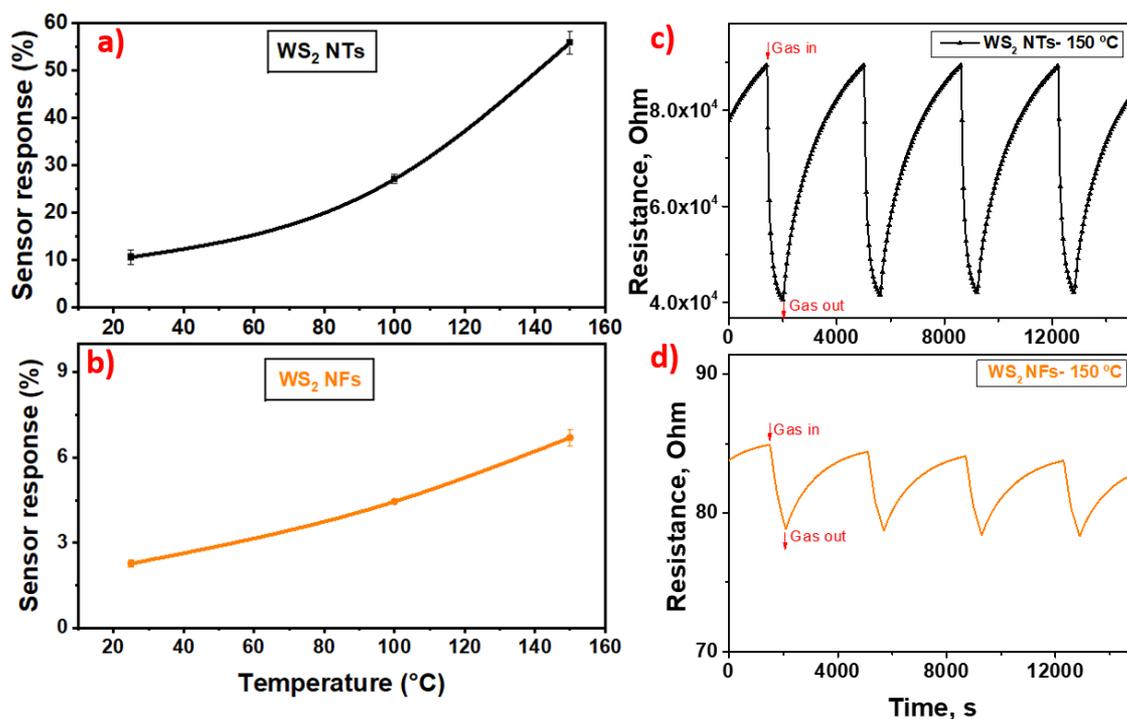
Fig. 7. (a and b) gas sensor response of WS$_2$ NTs and WS$_2$ NFs as a function of temperature, towards NO$_2$ at 800 ppb and 300 ppb, respectively and (c and d) electrical resistance change of both sensors operated at 150 ºC, towards these concentrations.
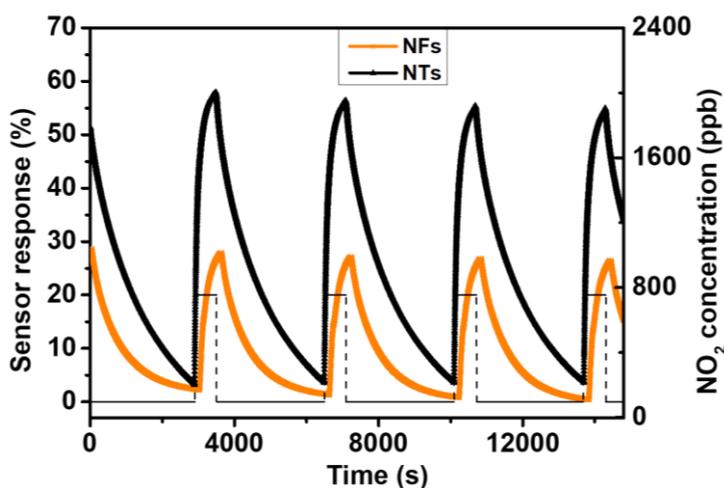

Fig. 8. WS$_2$ NFs (orange), WS$_2$ NTs (black) sensor responses (4 replicate response and recovery cycles) towards 800 ppb of NO$_2$ at the operating temperature of 150˚C.
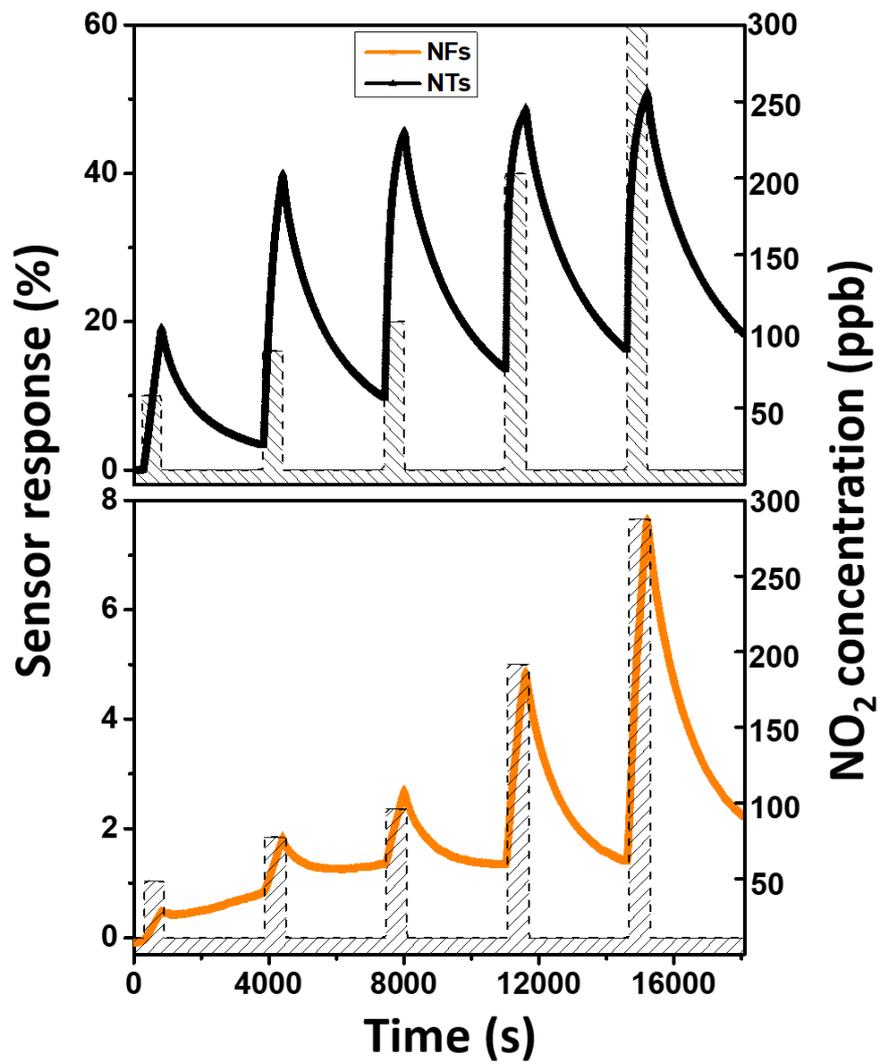
Fig. 9. WS₂ NF (orange), WS₂ NT (black) sensor response and recovery towards pulses of increasing concentrations of NO₂ gas (from 50 to 300 ppb). Sensors were operated at 150ºC.
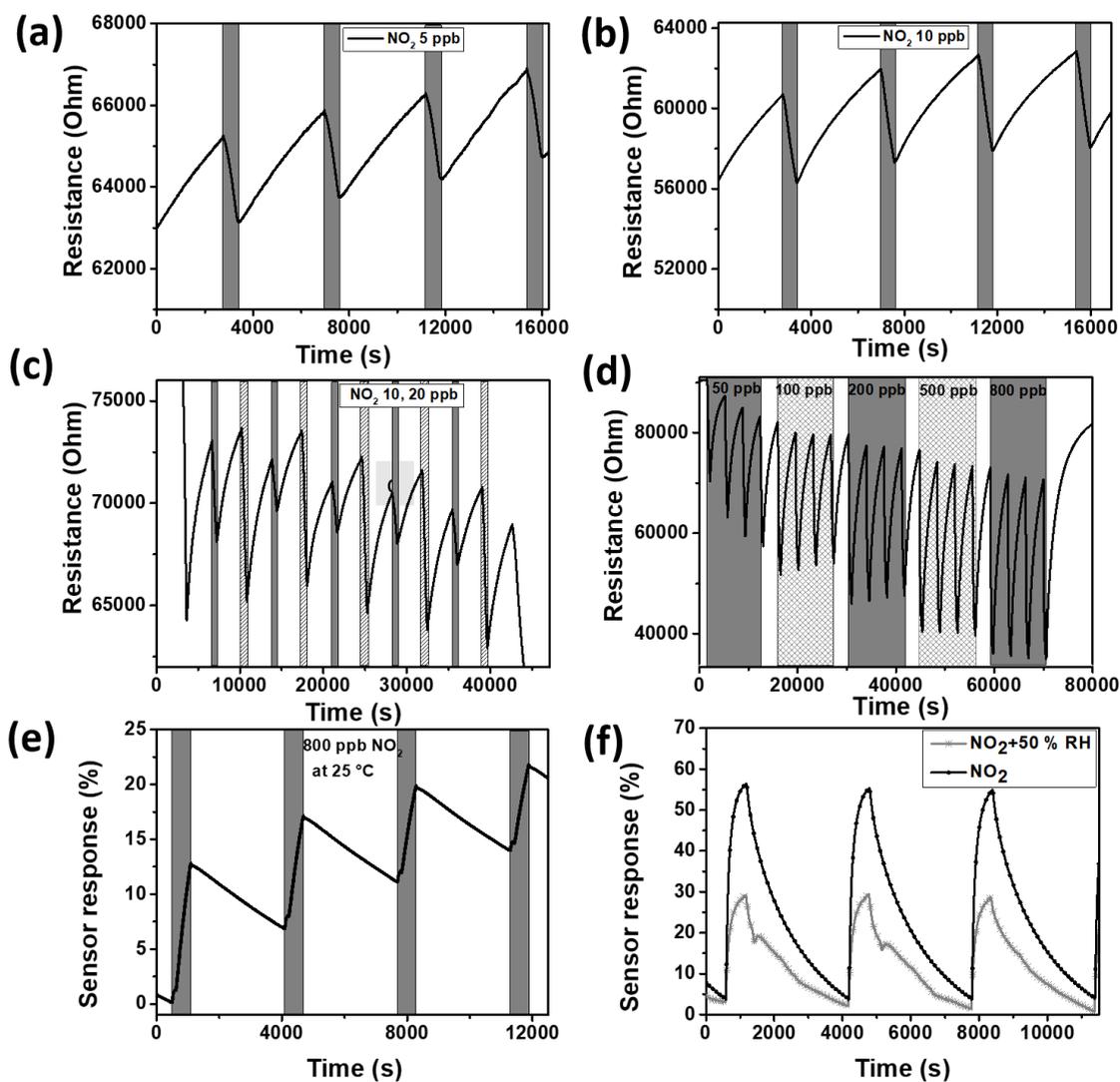
Fig. 10. Repeated response and recovery cycles for a WS_2 NT nanomaterial towards different concentrations of NO_2. Unless otherwise specified, the operating temperature was set to 150ºC. (a) 5 ppb; (b) 10 ppb; (c) five replicate measurements for consecutive 10 and 20 ppb pulses; (d) four replicate measurements for increasing concentration pulses ranging from 50 to 800 ppb; (e) four replicate measurements for 800 ppb pulses while operated at room temperature; (f) three replicate measurements for 800 ppb in dry and 50 % RH backgrounds.
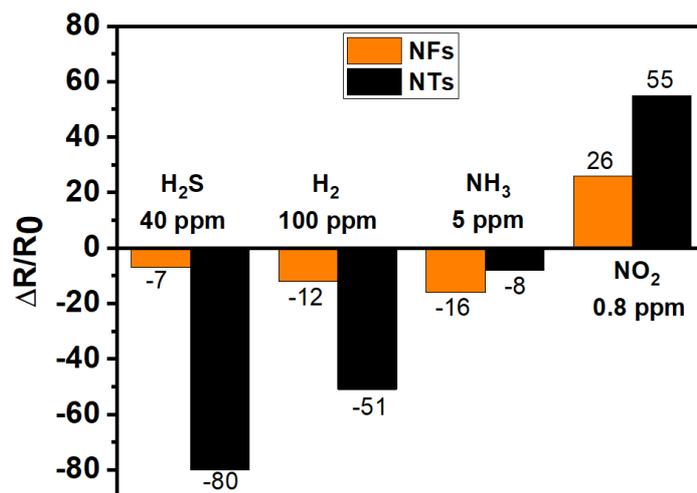
Fig. 11. Response histogram of WS$_2$ NFs and WS$_2$ NTs sensors operated at 150˚C.
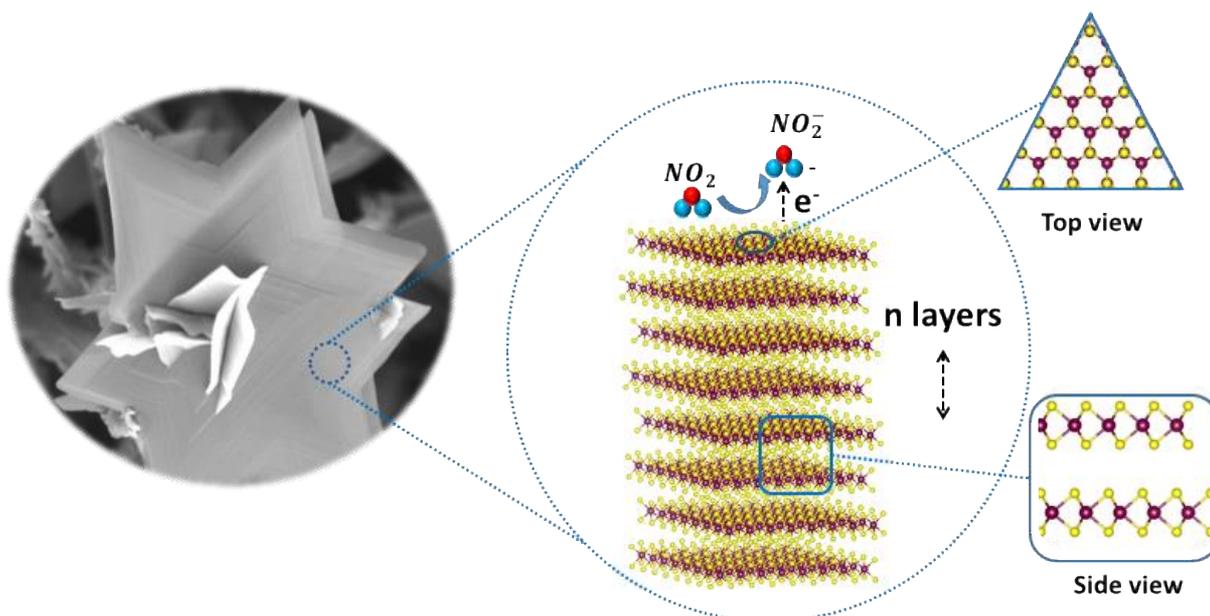
Fig. 12. Gas sensing mechanism of WS$_2$ nanosheets (W= pink, S= yellow) towards NO$_2$ gas molecules.

Table 1. Comparison of the sensing properties to NO_2 of resistive gas sensors based on different WS_2 sensing materials.

Structure	Working Temp. (˚C)	Studied Conc.	Response (%)	Sensitivity (Response%/ ppm)	Detection limit	Reference
Nanotriangles	150	800 ppb	55.9	70	< 5 ppb (experim.)	This work
Nanotriangles	25	800 ppb	10.6	13.2	N/A	This work
Nanoflakes	150	800 ppb	26.6	33.2	~50 ppb (experim.)	This work
Nanoflakes	25	300 ppb	0.5	1.7	N/A	This work
Nanosheets	NA	25 ppm	8.7	0.3	N/A	[26]
Nanosheets	25	5 ppm	68.4	13.7	0.1 ppm (experim)	[27]
Nanostructure (aerogel)	180	2 ppm	3	1.5	10 ppb (theoret.)	[28]
Nanostructure	25	5 ppm	2.5	0.5	N/A	[50]
Nanosheets	160	5 ppm	121	24,2	< 200 ppb (experim.)	[51]

N/A: Not available; experim.: experimentally measured; theoret.: theoretically calculated